ACS OMEGA

http://pubs.acs.org/journal/acsodf

Article

Favorable Role of the Metal–Support Perimeter Region in Electrochemical NH_3 Synthesis: A Density Functional Theory Study on $Ru/BaCeO_3$

Atsushi Ishikawa,* Fumiya Murase, Yoshitaka Tateyama, and Junichiro Otomo*

Cite This: *ACS Omega* 2022, 7, 26107–26115

Read Online

ACCESS | Metrics & More | Article Recommendations | Supporting Information

ABSTRACT: The catalytic electrochemical synthesis of NH_3 on $Ru/BaCeO_3$ was investigated using density functional theory. The competition between NH_3 formation and the hydrogen evolution reaction (HER) is a key for a high NH_3 formation rate. Our calculations show that H adsorbs more strongly than N_2 at the Ru particle moiety, while the adsorption of N_2 is stronger than the H adsorption at the $Ru/BaCeO_3$ perimeter, a model for the triple-phase boundary that is proposed to be an active site by experimental studies. This indicates that, while the HER is more favorable at the Ru particle moiety, it should be suppressed at the $Ru/BaCeO_3$ perimeter. We also calculated the Gibbs free energy changes along the NH_3 formation and found that the N_2H formation, the $NHNH_2$ formation, and the NH_3 formation steps have a relatively large Gibbs energy change. Therefore, these are possible candidates for the potential-determining step. The calculated equilibrium potential (U = −0.70 V, vs RHE) is in reasonable agreement with experiments. We also evaluated the reaction energy (ΔE) and the activation barrier (E_a) of the N_2H formation at several sites. ΔE and E_a were high at the Ru particle moiety (ΔE = 1.18 eV and E_a = 1.38 eV) but became low (ΔE = 0.32 eV and E_a = 1.31 eV) at the $Ru/BaCeO_3$ perimeter. These provide the atomic-scale mechanism how the proton conduction in $BaCeO_3$ assists the electrochemical NH_3 synthesis.

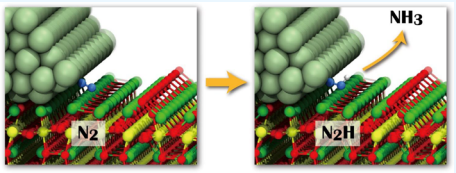

1. INTRODUCTION

Recently, ammonia (NH_3) has attracted considerable attention as a hydrogen (H_2) energy carrier for several reasons. First, NH_3 is much easier to liquefy and transport than H_2. Second, NH_3 has a higher volumetric H_2 density (120.3 kg-H_2·m^{-3}) than liquid H_2 (70.9 kg-H_2·m^{-3}) or toluene/methylcyclohexane (47.1 kg-H_2·m^{-3}).[1] Despite these advantages of NH_3 as a H_2 carrier, the Haber–Bosch process[2] remains the main synthetic route for producing NH_3 from N_2. However, the main hydrogen source for this process is currently the hydrogen gas formed from natural gas. This requires large amounts of energy; thus the NH_3 formation without using hydrogen from natural gas is highly desirable. For this purpose, electrochemical NH_3 synthesis is a promising approach because it utilizes H_2O as a hydrogen source.[3] Electrochemical NH_3 synthesis could be a key technology for a carbon-neutral society.

One promising approach for electrochemical NH_3 synthesis is to employ a fuel cell with a solid electrolyte. Many studies have reported using a solid electrolyte for NH_3 synthesis at the gas–solid interface.[4,5] This device consists of an anode, a cathode, and a solid electrolyte. The anode and cathode reactions are

$$H_2O \rightleftarrows \frac{1}{2}O_2 + 2H^+ + 2e^- \quad (1)$$

and

$$N_2 + 6H^+ + 6e^- \rightleftarrows 2NH_3 \quad (2)$$

respectively, and the net reaction is

$$N_2 + 3H_2O \rightleftarrows 2NH_3 + \frac{3}{2}O_2 \quad (3)$$

Water dissociation on the anode generates protons, which are transported to the cathode through the solid electrolyte and combine with electrons and N_2 there to produce NH_3. The NH_3 formation at the cathode is known to determine the overall reaction rate and yield, and extensive efforts have been devoted to finding effective catalysts for the cathode reaction. For example, several research groups have investigated metal systems such as Ru and Ni. Ru is well known as a suitable catalyst for NH_3 synthesis because it exhibits a high NH_3 formation rate.[6] However, the electrochemical NH_3 formation rates reported are still low, such as 3.0 × 10^{-13} mol·s^{-1}·cm^{-2} on Ru/MgO, as observed by Skodra and Stoukides.[7]

To further enhance the NH_3 formation rate for practical purposes, a detailed understanding of the reaction mechanism is necessary. Several mechanistic studies based on kinetic

Received: March 1, 2022
Accepted: June 20, 2022
Published: July 22, 2022

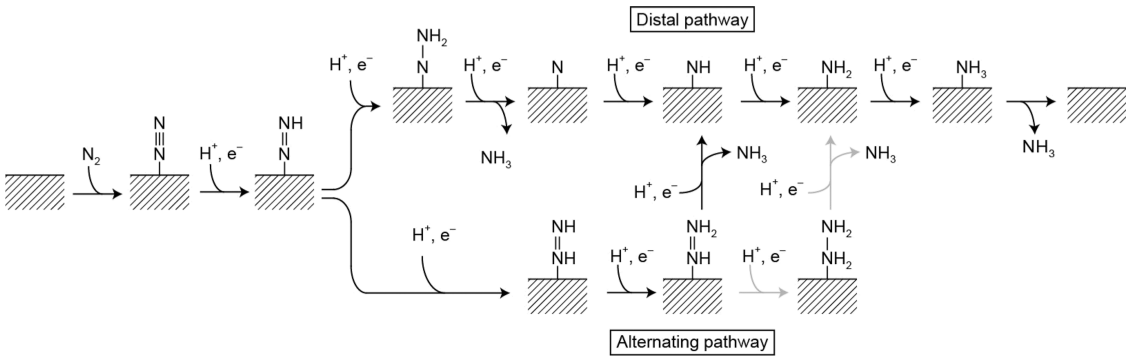

Figure 1. Schematic reaction mechanisms for associative NH_3 synthesis via distal and alternating pathways. The shaded area denotes the Ru surface. The alternating pathway has two further possibilities shown by the black and light gray arrows.

measurements or theoretical calculations have been performed.[3] Currently, there are two widely accepted pathways for NH_3 synthesis: the dissociative mechanism (in which N−N bond dissociation occurs first) and the associative mechanism (in which NH_x (x = 1−3) species form before N−N bond dissociation).[8−11] The Haber−Bosch process is considered to occur through the dissociative mechanism, while many researchers believe that electrochemical NH_3 synthesis occurs through an associative mechanism because of its milder reaction conditions.[9,12] Another important mechanism is the Mars−van Krevelen mechanism, in which lattice N atoms are used for NH_3 formation; several research groups have investigated electrochemical NH_3 synthesis via this mechanism using a metal nitride cathode.[3,13]

Another key factor in the electrochemical NH_3 synthesis is its competition with the hydrogen evolution reaction (HER).[5,14] This reaction is expressed as

$$2H^+ + 2e^- \rightleftarrows H_2 \quad (4)$$

H adsorption on the catalyst surface or active site competes with N_2 adsorption, and when a negative potential is applied, the HER becomes easier than NH_3 formation. This is unfavorable for the NH_3 formation because the active sites and the electronic current are consumed by the HER. Some catalyst systems with high N_2 dissociation rates (e.g., Ru and Ni) suffer from low NH_3 formation rates because of the HER; several groups previously analyzed the competition of the HER and NH_3 synthesis and have shown that overcoming the HER is necessary condition to have a high NH_3 formation rate.[12,15]

As stated above, many mechanistic insights into electrochemical NH_3 synthesis have been obtained. However, several important features remain uninvestigated, such as the metal−support interaction, which is known to play an important role in catalysis.[16] Indeed, the triple-phase boundary (TPB) is considered to be the active site for electrochemical NH_3 synthesis in the gas phase.[17] Therefore, identifying the detailed mechanism at the TPB is of particular importance. One of the authors of the present study found that, in the $Ru/BaCeO_3$ system, a smaller Ru particle size is favorable for electrochemical NH_3 synthesis because of the increased $Ru/BaCeO_3$ perimeter region, which has an NH_3 formation rate of 1.1×10^{-11} mol·s^{-1}·cm^{-2}.[17] Recently, we proposed the formation of an effective double layer during NH_3 electrosynthesis with $Fe/BaCeO_3$, which can be considered as an extension of the TPB active site model.[18] Several researchers have investigated the metal−support interaction in the electrochemical reaction and noted some similarities between this interaction and the electrochemical promotion effect.[19] An understanding of the complex relationship between these two factors is important for enhancing the electrochemical catalysis process. However, there is still much to be learned on this issue.

In this study, we theoretically investigated electrochemical NH_3 synthesis using a $Ru/BaCeO_3$ system. To the best of our knowledge, this is the first computational analysis of the metal−support interaction during electrochemical NH_3 synthesis. Our focus was the effect of the metal−support interaction on the mechanistic details, especially on the competition between NH_3 formation and the HER and the energetics of NH_3 formation. First-principles density functional theory (DFT) calculations were employed to provide a reliable description of the thermodynamic and kinetic properties. We first examined the competitive adsorption of H and N_2 on the Ru surface to identify the available active sites for NH_3 synthesis. Then, we investigated NH_3 formation by considering the free energy profiles under an applied electric potential. Based on the energetic profile of H and N_2 adsorption on the active sites, the availability of the sites, that is, competition between the HER and the NH_3 formation is discussed. The calculated free energy profile is compared with experimental results. Finally, we evaluated the activation barrier (E_a) of the N_2H formation step, identified as one of the key steps of electrochemical NH_3 formation from the analysis of the free energy profile.

2. METHOD

2.1. Reaction Model. For electrochemical NH_3 synthesis, two pathways have been discussed, namely, the dissociative and associative mechanisms.[10,11,20] With Ru catalysts, it is widely accepted that the dissociative mechanism mainly occurs at stepped surfaces.[8,21] However, the associative mechanism is more plausible for the current purpose from the following reasons: (1) considering the structure of the perimeter moiety, stepped surfaces are unlikely to be formed at the $Ru/BaCeO_3$ perimeter, and (2) NH_3 formation at the $Ru/BaCeO_3$ perimeter occurs under proton-rich conditions because a proton is always supplied through $BaCeO_3$. Note that the NH_3 formation on Ru nanoparticles (i.e., nonperimeter sites) can be modeled using a conventional Ru slab model. As such models have been extensively studied, we did not repeat the calculations.[11,12]

In addition to differences in the order of N−H bond formation and N_2 dissociation, there are two possibilities for the H addition to N or N_2: the Tafel mechanism and the Heyrovsky mechanism. In the former, the N−H bond is

https://doi.org/10.1021/acsomega.2c01222
ACS Omega 2022, 7, 26107−26115

formed between N and H atoms both adsorbed on the metal surface, while in the latter, the added H comes from a medium such as a gas, solvent, or solid electrolyte. Skúlason et al. compared these two mechanisms and concluded that the Heyrovsky mechanism is favorable in terms of the reaction energy.[12] Based on this, we considered the associative Heyrovsky mechanism, which involves the following elementary steps (the active site is denoted by an asterisk (*)):

$$N_2 + {}^* \rightleftarrows N_2{}^* \quad (5)$$

$$N_2{}^* + 6(H^+ + e^-) \rightleftarrows N_2H^* + 5(H^+ + e^-) \quad (6)$$

$$N_2H^* + 5(H^+ + e^-) \rightleftarrows N_2H_2{}^* + 4(H^+ + e^-) \quad (7)$$

$$N_2H_2{}^* + 4(H^+ + e^-) \rightleftarrows N^* + NH_3 + 3(H^+ + e^-) \quad (8)$$

$$N^* + 3(H^+ + e^-) \rightleftarrows NH^* + 2(H^+ + e^-) \quad (9)$$

$$NH^* + 2(H^+ + e^-) \rightleftarrows NH_2{}^* + (H^+ + e^-) \quad (10)$$

$$NH_2{}^* + (H^+ + e^-) \rightleftarrows NH_3{}^* \quad (11)$$

$$NH_3{}^* \rightleftarrows NH_3 + {}^* \quad (12)$$

For the associative Heyrovsky mechanism, Li et al. proposed two possible pathways depending on the position of H addition to the N_2H intermediate.[22] These pathways are denoted as the alternating and distal pathways in Figure 1.

The Gibbs free energy change for NH_3 electrosynthesis was analyzed using the approach proposed by Nørskov et al.[12,23] It was calculated as follows:

$$\Delta G(U) = \Delta E_{DFT} + \Delta E_{ZPE} - T\Delta S - neU \quad (13)$$

where ΔE_{DFT} is the reaction energy calculated using DFT; ΔE_{ZPE} and ΔS are the changes in the zero-point energy (ZPE) and entropy along the reaction step, respectively. U is the externally applied electric potential that shifts the Gibbs energy of the reaction intermediate by $-neU$ (n = number of electrons involved). The ZPE and the entropies of gaseous molecules (N_2, H_2, and NH_3) were obtained from experimental data and are listed in Table S1.[24] To calculate the chemical potential of the proton−electron pair ($H^+ + e^-$), we employed the computational hydrogen electrode model.[23] In this model, the Gibbs energy $G(H^+ + e^-)$ is equivalent to half of the Gibbs energy of gaseous hydrogen ($1/2G(H_2)$) under standard conditions (pH = 0, 298.15 K, 1 atm) with no external potential.

2.2. Computational Details. We employed the DFT + U method (DFT plus Hubbard-U parameter) for all DFT calculations.[25] The Perdew−Burke−Ernzerhof functional was used for the exchange-correlation functional.[26] The effective Hubbard-U parameter, that is, $U - J$ was set to 6.0 eV, which was used for the Ce 4f electrons as in a previous DFT + U study on $BaCeO_3$.[27] We examined the dependence of the results on the Hubbard-U parameter by using the N_2 adsorption energy on $Ru/BaCeO_3$ as a benchmark (Figure S1). When the U parameter was varied within 0.0−8.0 eV, the N_2 adsorption energy ranged from −0.47 to −0.51 eV. This indicates that the U parameter has only weak effects on the Gibbs free energy profiles.

We performed geometry optimization by fixing the lower two-thirds of the $BaCeO_3$ structure. The Ru moiety and the adsorbates were fully relaxed. Figure 2 displays details of the

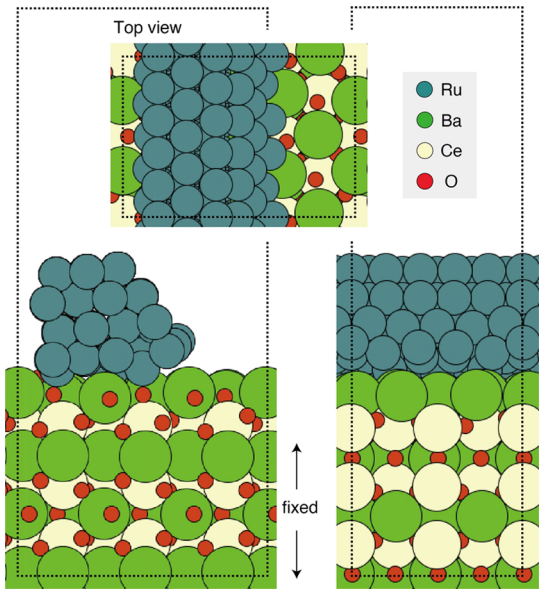

Figure 2. Top view and two-side views of the $Ru/BaCeO_3$ rod model used in the calculations. The lower two-thirds of $BaCeO_3$ were fixed during geometry optimization.

$Ru/BaCeO_3$ unit cell model, which contained 284 atoms, with 13 atomic layers of $BaCeO_3$ and 4 of Ru. No spatial symmetry was imposed in the calculations. To evaluate the ZPE, a vibrational analysis was performed using a finite difference of 0.015 Å and allowing only the adsorbate molecules to move. Unit cell optimization was performed for the $Ru/BaCeO_3$ system (without an adsorbate), and the optimized unit cell parameters were used for the subsequent calculations. For the surface energy calculations, another unit cell optimization was performed. For a selected case, we performed a molecular dynamics (MD) simulation with an NVT ensemble to search for a stable adsorbate structure. A Nose−Hoover thermostat was used there, the temperature was controlled at 500 K, and the simulation was carried out for 1 ps with a time step of 1 fs.

The core electrons were represented using the projector-augmented wave method.[28] The valence electrons were expanded by the plane wave basis set up to a cutoff energy (E_{cut}) of 400 eV. The electron occupation near the Fermi level was determined using the first-order Methfessel−Paxton scheme with σ = 0.1. The convergence criteria for the electronic state and geometry optimization calculations were set to 1.0×10^{-5} and 0.03 eV·Å^{-1} in energy and force, respectively. Transition state (TS) search was done with the climbing image nudged elastic band (CINEB) and the dimer methods.[29] The vibrational analysis of the TSs confirmed that they were the first-order saddle point in the potential energy surface. Reciprocal space integration was performed with the k-point placed using the Monkhorst−Pack scheme. The k-point mesh was set to $3 \times 3 \times 1$ for the surface calculations and to $9 \times 9 \times 9$ for the bulk material calculations. Gamma-point sampling ($1 \times 1 \times 1$) was used in the MD and CINEB calculations. A vacuum layer of ∼20 Å was introduced between the slabs. Bader charge analysis was used to investigate the electronic properties.[30] Dipole correction in the z-direction was applied in all calculations except when calculating the bulk material and isolated molecules. All DFT calculations were performed using the Vienna ab initio simulation package version 5.4.[31]

https://doi.org/10.1021/acsomega.2c01222
ACS Omega 2022, 7, 26107−26115

3. RESULTS AND DISCUSSION

3.1. Determination of the Most Stable Surface Termination. Herein, we employed perovskite $BaCeO_3$ as the proton-conducting electrolyte. Although a previous experimental study used yttrium-doped $BaCeO_3$ as the electrolyte,[17] the doping level was moderate ($BaCe_{0.9}Y_{0.1}O_3$) and was therefore not expected to change the reaction mechanism of NH_3 synthesis. The orthorhombic unit cell structure of $BaCeO_3$ was obtained from the Inorganic Crystal Structure Database (ICSD ID = 188637). First, we need to identify the most stable surface of $BaCeO_3$ among several candidates, because the surface should be exposed during electrochemical NH_3 synthesis. Previously, Shishkin and Ziegler employed the DFT method to compare the stabilities of the (100), (110), and (111) surfaces of $BaCeO_3$ and found (100) to be the most stable.[32] Based on their result, we considered the (100) surface of $BaCeO_3$ in this study.

We used a $2 \times 2 \times 2$ supercell to model the $BaCeO_3$ surface. The surface energy (E_{surf}) was evaluated as follows:

$$E_{surf} = \frac{1}{2A}\left[E_{slab} - \left\{N \cdot E_{bulk} + \sum_{X}^{Ce,O} \mu_X (n_{X,slab} - n_{X,bulk})\right\}\right] \quad (14)$$

where A is the surface area calculated from the optimized unit cell, E_{slab} is the total energy of the slab, E_{bulk} is the total energy of bulk $BaCeO_3$, $N = n_{Ba,\ slab}/n_{Ba,\ bulk}$ is the number of $BaCeO_3$ unit cells, and $n_{X,\ slab}$ and $n_{X,\ bulk}$ are the numbers of atom X in the slab and bulk models, respectively. μ_X is the chemical potential of atom X.[32,33] The chemical potential of an oxygen atom (μ_O) is calculated from

$$\mu_O = E_O + \frac{1}{2}BDE_{O_2} - ZPE \quad (15)$$

where E_O is the total energy of O atom, and BDE_{O_2} and ZPE are the bond dissociation energy and zero-point energy of O_2, respectively.[34] We employed the experimentally measured values of BDE_{O_2} = 4.89 eV and ZPE = 0.10 eV.[24] For the total energy calculation of O atom, DFT calculations were performed using B3LYP as the exchange-correlation functional.

The chemical potentials of Ce and Ba were evaluated as

$$\mu_{Ce} = E_{CeO_2} - 2\mu_O \quad (16)$$

$$\mu_{Ba} = E_{BaO} - \mu_O \quad (17)$$

where the references for Ce and Ba were bulk CeO_2 and BaO, respectively. The total energies (E_{CeO2} and E_{BaO}) were evaluated using DFT. The initial structures of CeO_2 and BaO were obtained from the ICSD (ID = 88759 and 616005, respectively). The calculated chemical potentials of H, O, Ce, and Ba are listed in Table S2. Using these quantities, we calculated the surface energies with four different terminations: CeO_2 termination, CeO_2−O termination, BaO termination, and BaO−O termination (see Figure S2 for their surface structures). According to the calculated E_{surf} values in Table 1, BaO termination is the most stable. Based on this result, we constructed the $Ru/BaCeO_3$ rod model to represent the $Ru/BaCeO_3$ perimeter. We placed a Ru rod consisting of 80 atoms on this surface. The resultant structure is shown in Figure 2. This model is used in the NH_3 synthesis at the $Ru/BaCeO_3$ perimeter, which will be discussed in the following sections.

Table 1. Surface Energies (E_{surf}) of $BaCeO_3$(100) Surfaces with Different Terminations, as Calculated Using DFT

	CeO_2	CeO_2−O	BaO	BaO−O
surface energy ($J \cdot m^{-2}$)	1.38	4.75	1.03	4.34

3.2. Competitive Adsorption of H and N_2. As discussed in Introduction, one reason for a low NH_3 formation rate is competition with the HER. In this subsection, we investigated the adsorption of H and N_2 on $Ru/BaCeO_3$. We consider the adsorption of H and N_2 to occur on the several sites on the Ru rod (top, edge, side) and the $Ru/BaCeO_3$ perimeter sites. The top part of the Ru rod has a surface structure similar to that of Ru(0001); therefore, we assume that this part has a reactivity similar to that of the Ru surface or nanoparticles. Figure 3 summarizes Gibbs free energies of H and N_2 adsorption (ΔG_{ad}), together with the optimized geometries. First, we discuss N_2 and H adsorption on the top part of the Ru rod. At this location, N_2 undergoes atop adsorption, while H adsorption is exergonic at both the fcc and hcp threefold hollow sites. Notably, N_2 adsorption on the top part is weak, as indicated by the positive ΔG_{ad} value (0.08 eV); this is in agreement with the previously reported tendency on Ru(0001).[12] On the other hand, H adsorption is strong (ΔG_{ad} = −0.36 eV) on the Ru particle, suppressing NH_3 formation at these locations through serious H poisoning. A similar tendency was observed for H and N_2 adsorption on the upper edge part. Among the Ru edge or side part of the rod, the H adsorption is most strong at the edge site with bridge type adsorption (ΔG_{ad} = −0.59 eV). The H adsorption on this site is stronger than the H adsorption on the Ru top part. N_2 adsorption here is much weaker than the H adsorption (ΔG_{ad} = −0.29 eV), although still stronger than that at the Ru top part.

Next, we consider N_2 and H adsorption on the $Ru/BaCeO_3$ perimeter. Here, H adsorption is the strongest at the bridge site (bridge(A) in Figure 3), as its ΔG_{ad} is −0.79 eV; it is much stronger than that on the Ru top or edge parts. The strongest N_2 adsorption on $Ru/BaCeO_3$ occurs at the atop(A) site with side-on adsorption mode, as its ΔG_{ad} is −1.02 eV. In this configuration, two Ru atoms at the perimeter are used, where each N atom binds different Ru atoms as shown in the top view (Figure 3). This adsorption mode is close to the enzymatic configuration (N*−N*), which is seen in the N_2 adsorption on the enzyme nitrogenaze.[35] Another mode of N_2 adsorption, atop adsorption, is also strong as its ΔG_{ad} is −0.64 eV. This is also much stronger than the N_2 adsorption on the Ru top and edge parts.

Thus, these results show that the N_2 adsorption at the $Ru/BaCeO_3$ perimeter is stronger than the H adsorption, which differs from the scenario at the Ru top or edge parts. To examine the stability of this N_2 adsorption site, we performed an MD simulation at T = 500 K up to 1 ps (see Figure S3 for the energy and geometry changes along the MD trajectory). Our MD calculation showed that N_2 is always adsorbed on the $Ru/BaCeO_3$ perimeter region. Thus, we can conclude that this site binds N_2 with considerable strength.

To analyze the electronic properties of the $Ru/BaCeO_3$ system, we carried out Bader charge analysis. The calculated charges of the Ru rod are summarized in Figure S4. The results show that the Ru atoms in the $Ru/BaCeO_3$ perimeter region are more negatively charged (∼ −0.2 e) than those in other parts of the Ru rod. This could lead to stronger adsorption of H and N_2 on the perimeter sites due to the possibility of

https://doi.org/10.1021/acsomega.2c01222
ACS Omega 2022, 7, 26107−26115

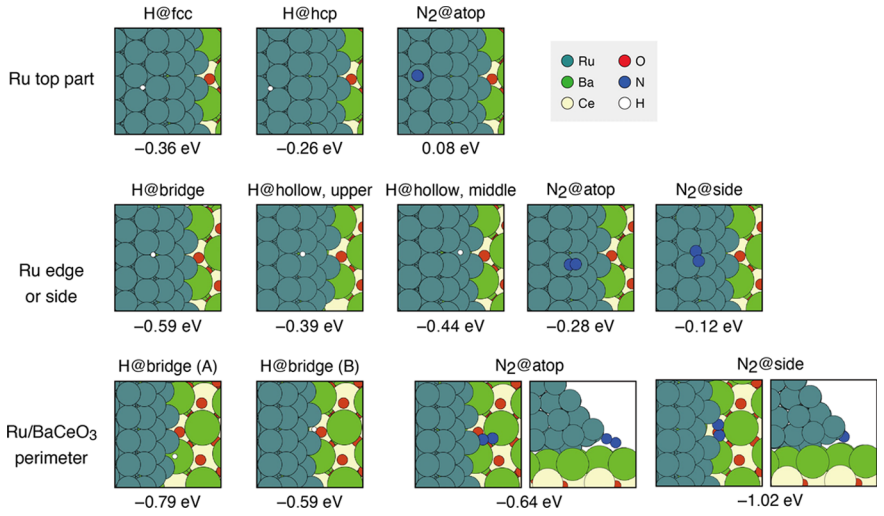

Figure 3. Optimized structures (top view) of H- and N_2-adsorbed $Ru/BaCeO_3$ systems and their adsorption energies. A side view is also provided for N_2 adsorption on the $Ru/BaCeO_3$ perimeter site.

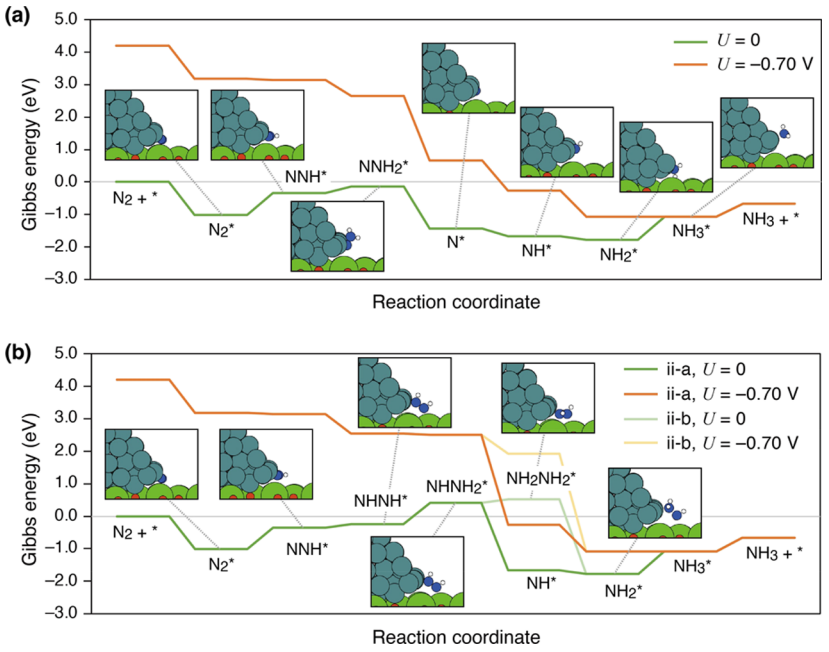

Figure 4. Gibbs free energy profiles at $U = 0$ and -0.70 V (Gibbs free energy of the PDE, the NH_3* formation step) during electrochemical NH_3 synthesis via (a) distal pathway, and (b) alternating pathway. In (b), two pathways are shown; (ii-a) alternating pathway without NH_2NH_2* formation, and (ii-b) alternating pathway with NH_2NH_2* formation. The temperature was set to 298.15 K. The inset images show the optimized structures.

stronger electrostatic interactions or back-donation to N_2 π* orbitals. This interaction is expected to enhance N_2 adsorption on the perimeter site, which is a unique feature not found in the Ru top or edge parts. This result strongly indicates that H_2 and N_2 adsorption is promoted on the TPB compared with that at other parts of the catalyst surface.

3.3. Gibbs Energy Changes during NH_3 Formation. Next, we investigated the Gibbs energy changes during NH_3 formation. Because the previous section concluded that N_2 most strongly interacts with the $Ru/BaCeO_3$ perimeter site, we consider it the active site for NH_3 formation. Figure 4 summarizes the Gibbs energy changes during NH_3 formation on $Ru/BaCeO_3$, considering both the distal and alternating pathways of NH_3 formation. The alternating pathway also includes two possible routes, namely $NHNH_2$* to NH* via NH_3 formation and desorption, or $NHNH_2$* to NH_2NH_2* formation. Therefore, we can propose three pathways for the NH_3 formation, that is, (i) the distal pathway, (ii-a) the alternating pathway without NH_2NH_2* formation, and (ii-b) the alternating pathway with NH_2NH_2* formation. These pathways are shown in Figure 4b, where the insets display the optimized structures for each step.

Based on our calculation, the elementary reactions with large ΔG values are N_2H* formation from N_2* (ΔG = 0.67 eV), $NHNH_2$* formation from NHNH* in path (ii-a) (ΔG = 0.66 eV), and NH_3* formation from NH_2* (ΔG = 0.70 eV). Therefore, these are possible candidate for the potential-determining step (PDS, i.e., the elementary step that requires the largest ΔG). Because the N_2H* formation and NH_3* formation appear in all the paths, it is difficult to conclude

https://doi.org/10.1021/acsomega.2c01222
ACS Omega 2022, 7, 26107−26115

whether the distal or alternating pathway is favorable. However, we could exclude the (ii-b) pathway because the NH_2NH_2* state is more thermodynamically unfavorable than the NH state. Note that the last reaction step, that is, the NH_3* desorption process is endergonic in Figure 4, but this process becomes exergonic by 0.57 eV at T = 500 °C, which corresponds to the experimental reaction temperature.[17] Therefore, the NH_3* desorption does not hinder the NH_3 formation.

The theoretical overpotential can be calculated from this ΔG value by applying an external potential U to make ΔG = 0 for the PDS. Figure 4 also shows the Gibbs energy changes under U = −0.70 V (vs RHE), which corresponds to the ΔG of NH_3* formation from NH_2*. One of the present authors reported in the experimental work that NH_3 electrosynthesis can be initiated by applying a potential of approximately −0.3 V.[17] Thus, the present calculation exhibits semiquantitative agreement with the experimental result, although it moderately overestimates the overpotential. Our calculated overpotential value is similar to that reported by Back and Jung (−0.68 V), who considered a Ru step as the active site.[11] Therefore, the $Ru/BaCeO_3$ perimeter site is not likely to reduce the overpotential for NH_3 synthesis.

In summary, the calculated Gibbs energy profiles have shown that (i) the PDS of the electrochemical NH_3 synthesis is the NH_3* formation step (NH_2* + H^+ + e^- ⇌ NH_3*), while the N_2H* formation step (N_2* + H^+ + e^- ⇌ N_2H*) or the $NHNH_2$* formation step (NHNH* + H^+ + e^- ⇌ $NHNH_2$*) has a similar ΔG value; thus these two are the possible candidate for the PDS, (ii) NH_3 synthesis can occur at the $Ru/BaCeO_3$ perimeter site upon applying a weak external potential, and this site is less vulnerable to H poisoning than the Ru top part is. Because we used the $Ru/BaCeO_3$ perimeter site to model the TPB of the solid electrolyte, the DFT results indicate that the presence of the TPB is favorable for NH_3 formation compared with the HER, from the thermodynamic viewpoint. In the next section, we further investigate the effect of the $Ru/BaCeO_3$ perimeter on the kinetics of NH_3 formation.

3.4. Reaction Path for the N_2H Formation Process.

The Gibbs energy analysis in the previous section has shown that N_2H formation is a key step in the NH_3 electrosynthesis, because it is involved in both distal and alternating pathways and has relatively large ΔG. Therefore, the kinetic parameters such as activation energy (E_a) or reaction energy (ΔE) for this process would be a governing factor for the NH_3 formation rate. In this section, we analyze how the $Ru/BaCeO_3$ boundary affects these parameters of the N_2H formation. We investigated three pathways for N_2H formation: I) at the Ru particle edge site, II) in the $Ru/BaCeO_3$ boundary region, between the N_2 molecule and H atom, both adsorbed on the Ru perimeter sites, and III) in the $Ru/BaCeO_3$ boundary region, between a N_2 molecule adsorbed on the Ru perimeter site and the H atom occupied the octahedral site in $BaCeO_3$. We considered the path III because $BaCeO_3$ is the proton-conducting solid electrolyte; thus the proton supply to the $BaCeO_3$ surface is possible. The optimized structures for the reactants, TSs, and product states for the three pathways are shown in Figure 5, together with the corresponding ΔE and E_a values. All the TSs are confirmed to have one imaginary frequency; see Table S3 for the calculated vibrational frequencies.

Figure 5 shows that N_2H formation via pathway I has E_a = 1.38 eV and is highly endothermic (ΔE = 1.18 eV). Thus,

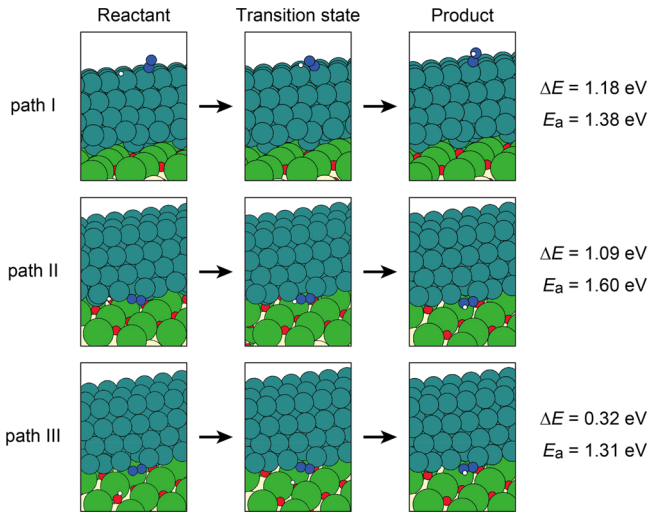

Figure 5. Reactant states, TSs, and product states for N_2H formation. Three reaction pathways were considered; (I) N_2H formation at the Ru particle edge site, (II) in the $Ru/BaCeO_3$ boundary region, between N_2 and H both adsorbed on the Ru perimeter sites, and (III) in the $Ru/BaCeO_3$ boundary region, between N_2 adsorbed on the Ru perimeter site and H occupying the octahedral site in $BaCeO_3$. ΔE and E_a values (including ZPEs) are shown together with the optimized structures.

when N_2 is adsorbed on the Ru edge site, N_2H formation is quite slow. In addition, our adsorption energy calculation (in Section 3.2) shows that the H atom adsorbs more strongly than N_2 at the edge site. Therefore, the active site is predominantly covered with H atoms (and thus more of the HER occurs), and N_2H formation at the Ru particle is unfavorable.

Next, we consider the pathway II. As shown in Section 3.2, the adsorption energies of N_2 and H at the Ru perimeter site are comparable; thus N_2H formation from this site is highly probable. However, our calculations show that the reaction requires a relatively large E_a (1.60 eV) and ΔE (1.09 eV). Note that the calculated N_2H formation Gibbs energy was 0.67 eV, where the coadsorption of N_2 and H was not accounted. The ΔE value of the pathway II includes the coadsorption effect, and this indicates that the adsorption of H considerably stabilizes the reactant state for N_2H formation. As a result, ΔE becomes larger than that in Figure 4. These results indicate that N_2H formation at the Ru perimeter site is slow, even when N_2 is strongly adsorbed on the Ru perimeter site.

Another possibility for N_2H formation at the $Ru/BaCeO_3$ boundary region is pathway III, that is, N_2H formation between N_2 at the Ru perimeter and the H atom from $BaCeO_3$. Although several positions of the H atom are possible in $BaCeO_3$, we selected the octahedral site of Figure 5 as it is closest to the surface. Figure 5 shows that pathway III has lower E_a (1.31 eV) and ΔE (0.32 eV) values compared with pathways I and II. Because the product state of N_2H formation is the same as that of pathway II, N_2H formation in the $Ru/BaCeO_3$ boundary region is more favorable when it occurs between an N_2 molecule on the Ru perimeter and H atom conducted from $BaCeO_3$. This computational result indicates that the proton-conducting support materials such as $BaCeO_3$ are kinetically favorable because they open a new pathway that accelerates the formation of N_2H.

https://doi.org/10.1021/acsomega.2c01222
ACS Omega 2022, 7, 26107−26115

4. CONCLUSIONS

Electrochemical NH_3 synthesis using a solid electrolyte is a promising approach for environmentally friendly NH_3 production. Previous experimental investigations of electrochemical NH_3 synthesis in the Ru/$BaCeO_3$ demonstrated the Ru/$BaCeO_3$ perimeter region (or three-phase boundary) to be the active site. In the present study, we used DFT calculations of a Ru rod model supported by $BaCeO_3$ to investigate electrochemical NH_3 synthesis and clarify the contribution of the metal−support interaction. First, after considering the $BaCeO_3$(100) surface with four different terminations, the surface with the Ba termination was determined to be the most stable as it had the lowest surface energy.

We then compared the adsorption of H and N_2 at several sites in the Ru/$BaCeO_3$ system, because this is a key factor influencing the two competitive reactions, that is, NH_3 formation and the HER. Because our calculated Gibbs energy of adsorption (ΔG_{ad}) shows that H adsorbed more strongly than N_2 at the top part of the Ru particle, the HER is considered more favorable at that site, which corroborates previous reports. In contrast, N_2 has stronger adsorption (ΔG_{ad} = −1.02 eV) than the H atom (ΔG_{ad} = −0.79 eV) at the Ru/$BaCeO_3$ perimeter site. This suggests the weaker hydrogen poisoning on the Ru/$BaCeO_3$ perimeter site, which is favorable for the NH_3 formation.

Assuming the Ru/$BaCeO_3$ perimeter as the active site, we also calculated the Gibbs free energy changes along NH_3 formation; the associative mechanism (N_2H_x formation prior to N−N dissociation) was assumed. Our results indicate that the PDS for NH_3 formation is either the NH_3* formation step (ΔG = 0.70 eV) or the N_2H* formation step (ΔG = 0.67 eV). Accordingly, the theoretical equilibrium potential is U = −0.70 V, which is in reasonable agreement with the experimental value. This value is similar to the previously reported value for the pure Ru model. Considering these DFT results, the Ru/$BaCeO_3$ perimeter site is favorable for the electrochemical NH_3 synthesis because the HER is inhibited there and not because of the decrease in the overpotential of the NH_3 formation. We also located the TS for the potential-determining N_2H formation step. Our calculated activation barriers showed that N_2H formation in the Ru/$BaCeO_3$ boundary region is favorable, especially when N_2 at the Ru perimeter site reacts with an H atom from $BaCeO_3$. Thus, a faster rate for N_2H formation is expected in the Ru/$BaCeO_3$ perimeter region.

This investigation is the first to confirm theoretically that electrochemical NH_3 synthesis is favorable at the TPB. The proton-conducting nature of $BaCeO_3$ is beneficial for the NH_3 formation because (i) it supplies the N_2 activation site that has some resistance to the hydrogen poisoning, (ii) it assists the N_2H formation by lowering the activation barrier, and (iii) it helps the supply of the reactant species (H atom in the present case). We consider that such a metal−support interaction might be a clue for increasing the NH_3 formation rate. Our theoretical analysis strongly implies that enlarging this area is beneficial for electrochemical NH_3 synthesis, from the above reasons. Based on this idea, detailed catalyst designs at the interface could enhance the reaction rate of electrochemical NH_3 synthesis.

■ ASSOCIATED CONTENT

Supporting Information

The Supporting Information is available free of charge at https://pubs.acs.org/doi/10.1021/acsomega.2c01222.

Table S1: Thermal corrections and ZPEs taken from experimental values, Table S2: Calculated chemical potentials for Ce, Ba, and O, Table S3: Vibrational frequencies for the TS geometries in Figure 5, Figure S1: Effect of the U parameter in the DFT + U scheme on N_2 adsorption energy (in eV) in the Ru/$BaCeO_3$ system, Figure S2: Optimized structures of $BaCeO_3$(100) surfaces with four different terminations, Figure S3: Energy and geometry changes along the MD trajectory for N_2 binding on the Ru/$BaCeO_3$ perimeter site, and Figure S4: Bader charges of the Ru rod in the Ru/$BaCeO_3$ model (PDF)

■ AUTHOR INFORMATION

Corresponding Authors

Atsushi Ishikawa − *Center for Green Research on Energy and Environmental Materials (GREEN), National Institute for Materials Science (NIMS), Tsukuba, Ibaraki 305-0044, Japan; Elements Strategy Initiative for Catalysts & Batteries (ESICB), Kyoto University, Kyoto 615-8510, Japan;* orcid.org/0000-0001-6908-831X; Email: ISHIKAWA.Atsushi@nims.go.jp

Junichiro Otomo − *Department of Environment Systems, Graduate School of Frontier Sciences, The University of Tokyo, Kashiwa, Chiba 277-8563, Japan; Department of Transdisciplinary Science and Engineering, School of Environment and Society, Tokyo Institute of Technology, Tokyo 152-8550, Japan;* orcid.org/0000-0002-3179-8284; Email: otomo@tse.ens.titech.ac.jp

Authors

Fumiya Murase − *Department of Environment Systems, Graduate School of Frontier Sciences, The University of Tokyo, Kashiwa, Chiba 277-8563, Japan*

Yoshitaka Tateyama − *Center for Green Research on Energy and Environmental Materials (GREEN), National Institute for Materials Science (NIMS), Tsukuba, Ibaraki 305-0044, Japan; Elements Strategy Initiative for Catalysts & Batteries (ESICB), Kyoto University, Kyoto 615-8510, Japan; International Center for Materials Nanoarchitectonics (MANA), NIMS, Tsukuba, Ibaraki 305-0044, Japan;* orcid.org/0000-0002-5532-6134

Complete contact information is available at: https://pubs.acs.org/10.1021/acsomega.2c01222

Author Contributions

The manuscript was written through the contributions of all the authors. All authors approved the final version of the manuscript.

Notes

The authors declare no competing financial interest.

■ ACKNOWLEDGMENTS

This study was supported in part by JSPS KAKENHI (Grant Number JP16762460), MEXT under the Elementary Strategy Initiative (Grant Number JPMXP0112101003), and the Program for Promoting Research on the Supercomputer Fugaku (Fugaku Battery & Fuel Cell Project) (Grant Number

JPMXP1020200301). The calculations were carried out at the supercomputer center of NIMS, Kyushu University (ITO), and Hokkaido University (Grand Chariot). This work was supported in part by the K computer at RIKEN AICS through the HPCI System Research Projects (Proposal nos. hp170174 and hp180115). The discussion of the reaction mechanism in this study is also based on research supported by JST CREST (Grant Number JPMJCR1441) and JSPS KAKENHI (Grant Number 21H04938).

REFERENCES

(1) Wijayanta, A. T.; Oda, T.; Purnomo, C. W.; Kashiwagi, T.; Aziz, M. Liquid Hydrogen, Methylcyclohexane, and Ammonia as Potential Hydrogen Storage: Comparison Review. *Int. J. Hydrogen Energy* **2019**, *44*, 15026−15044.

(2) Liu, H. *Ammonia Synthesis Catalysts: Innovation and Practice*; World Scientific/Chemical Industry Press, 2013.

(3) (a) Kyriakou, V.; Garagounis, I.; Vasileiou, E.; Vourros, A.; Stoukides, M. Progress in the Electrochemical Synthesis of Ammonia. *Catal. Today* **2017**, *286*, 2−13. (b) Cui, X.; Tang, C.; Zhang, Q. A Review of Electrocatalytic Reduction of Dinitrogen to Ammonia under Ambient Conditions. *Adv. Energy Mater.* **2018**, *8*, No. 1800369.

(4) (a) Marnellos, G.; Stoukides, M. Ammonia Synthesis at Atmospheric Pressure. *Science* **1998**, *282*, 98. (b) Ouzounidou, M.; Skodra, A.; Kokkofitis, C.; Stoukides, M. Catalytic and Electrocatalytic Synthesis of NH_3 in a H^+ Conducting Cell by Using an Industrial Fe Catalyst. *Solid State Ionics* **2007**, *178*, 153−159. (c) Amar, I. A.; Lan, R.; Humphreys, J.; Tao, S. Electrochemical Synthesis of Ammonia from Wet Nitrogen via a Dual-Chamber Reactor Using $La_{0.6}Sr_{0.4}Co_{0.2}Fe_{0.8}O_{3-\delta}$-$Ce_{0.8}Gd_{0.18}Ca_{0.02}O_{2-\delta}$ Composite Cathode. *Catal. Today* **2017**, *286*, 51−56.

(5) Kordali, V.; Kyriacou, G.; Lambrou, C. Electrochemical Synthesis of Ammonia at Atmospheric Pressure and Low Temperature in a Solid Polymer Electrolyte Cell. *Chem. Commun.* **2000**, *17*, 1673−1674.

(6) Ozaki, A.; Aika, K.-I.; Hori, H. A New Catalyst System for Ammonia Synthesis. *Bull. Chem. Soc. Jpn.* **1971**, *44*, 3216−3216.

(7) Skodra, A.; Stoukides, M. Electrocatalytic Synthesis of Ammonia from Steam and Nitrogen at Atmospheric Pressure. *Solid State Ionics* **2009**, *180*, 1332−1336.

(8) Dahl, S.; Logadottir, A.; Egeberg, R. C.; Larsen, J. H.; Chorkendorff, I.; Tornqvist, E.; Nørskov, J. K. Role of Steps in N_2 Activation on Ru(0001). *Phys. Rev. Lett.* **1999**, *83*, 1814−1817.

(9) Rod, T. H.; Logadottir, A.; Norskov, J. K. Ammonia Synthesis at Low Temperatures. *J. Chem. Phys.* **2000**, *112*, 5343−5347.

(10) Honkala, K.; Hellman, A.; Remediakis, I. N.; Logadottir, A.; Carlsson, A.; Dahl, S.; Christensen, C. H.; Nørskov, J. K. Ammonia Synthesis from First-Principles Calculations. *Science* **2005**, *307*, 555−558.

(11) Back, S.; Jung, Y. On the Mechanism of Electrochemical Ammonia Synthesis on the Ru Catalyst. *Phys. Chem. Chem. Phys.* **2016**, *18*, 9161−9166.

(12) Skúlason, E.; Bligaard, T.; Gudmundsdóttir, S.; Studt, F.; Rossmeisl, J.; Abild-Pedersen, F.; Vegge, T.; Jónsson, H.; Nørskov, J. K. A Theoretical Evaluation of Possible Transition Metal Electro-Catalysts for N_2 Reduction. *Phys. Chem. Chem. Phys.* **2012**, *14*, 1235−1245.

(13) (a) Abghoui, Y.; Garden, A. L.; Hlynsson, V. F.; Björgvinsdóttir, S.; Ólafsdóttir, H.; Skúlason, E. Enabling Electrochemical Reduction of Nitrogen to Ammonia at Ambient Conditions Through Rational Catalyst Design. *Phys. Chem. Chem. Phys.* **2015**, *17*, 4909−4918. (b) Abghoui, Y.; Garden, A. L.; Howalt, J. G.; Vegge, T.; Skúlason, E. Electroreduction of N_2 to Ammonia at Ambient Conditions on Mononitrides of Zr, Nb, Cr, and V: A DFT Guide for Experiments. *ACS Catal.* **2016**, *6*, 635−646.

(14) Lan, R.; Irvine, J. T. S.; Tao, S. Synthesis of Ammonia Directly From Air and Water at Ambient Temperature and Pressure. *Sci. Rep.* **2013**, *3*, 1145.

(15) Choi, C.; Back, S.; Kim, N.-Y.; Lim, J.; Kim, Y.-H.; Jung, Y. Suppression of Hydrogen Evolution Reaction in Electrochemical N2 Reduction Using Single-Atom Catalysts: A Computational Guideline. *ACS Catal.* **2018**, *8*, 7517−7525.

(16) Campbell, C. T. Catalyst-Support Interactions Electronic Perturbations. *Nat. Chem.* **2012**, *4*, 597−598.

(17) Kosaka, F.; Nakamura, T.; Otomo, J. Electrochemical Ammonia Synthesis Using Mixed Protonic-Electronic Conducting Cathodes with Exsolved Ru-Nanoparticles in Proton Conducting Electrolysis Cells. *J. Electrochem. Soc.* **2017**, *164*, F1323−F1330.

(18) Li, C.-I.; Matsuo, H.; Otomo, J. Effective Electrode Design and the Reaction Mechanism for Electrochemical Promotion of Ammonia Synthesis using Fe-Based Electrode Catalysts. *Sustainable Energy Fuels* **2021**, *5*, 188−198.

(19) (a) Nicole, J.; Tsiplakides, D.; Pliangos, C.; Verykios, X. E.; Comninellis, C.; Vayenas, C. G. Electrochemical Promotion and Metal−Support Interactions. *J. Catal.* **2001**, *204*, 23−34. (b) Vayenas, C. G.; Brosda, S.; Pliangos, C. The Double-Layer Approach to Promotion, Electrocatalysis, Electrochemical Promotion, and Metal−Support Interactions. *J. Catal.* **2003**, *216*, 487−504.

(20) (a) Rod, T. H.; Hammer, B.; Nørskov, J. K. Nitrogen Adsorption and Hydrogenation on a MoFe-6S-9 Complex. *Phys. Rev. Lett.* **1999**, *82*, 4054−4057. (b) Rod, T. H.; Nørskov, J. K. Modeling the Nitrogenase FeMo Cofactor. *J. Am. Chem. Soc.* **2000**, *122*, 12751−12763.

(21) Ishikawa, A.; Doi, T.; Nakai, H. Catalytic Performance of Ru, Os, and Rh Nanoparticles for Ammonia Synthesis: A Density Functional Theory Analysis. *J. Catal.* **2018**, *357*, 213−222.

(22) Li, X.-F.; Li, Q.-K.; Cheng, J.; Liu, L.; Yan, Q.; Wu, Y.; Zhang, X.-H.; Wang, Z.-Y.; Qiu, Q.; Luo, Y. Conversion of Dinitrogen to Ammonia by FeN_3-Embedded Graphene. *J. Am. Chem. Soc.* **2016**, *138*, 8706−8709.

(23) Nørskov, J. K.; Rossmeisl, J.; Logadottir, A.; Lindqvist, L.; Kitchin, J. R.; Bligaard, T.; Jonsson, H. Origin of the Overpotential for Oxygen Reduction at a Fuel-Cell Cathode. *J. Phys. Chem. B* **2004**, *108*, 17886−17892.

(24) *CRC Handbook of Chemistry and Physics*; CRC Press, 2014. *NIST Chemistry WebBook, NIST Standard Reference Database Number 69*. National Institute of Standards and Technology, 2021. https://doi.org/10.18434/T4D303

(25) Dudarev, S. L.; Botton, G. A.; Savrasov, S. Y.; Humphreys, C. J.; Sutton, A. P. Electron-Energy-Loss Spectra and the Structural Stability of Nickel Oxide: An LSDA+U Study. *Phys. Rev. B* **1998**, *57*, 1505−1509.

(26) Perdew, J. P.; Burke, K.; Ernzerhof, M. Generalized Gradient Approximation Made Simple. *Phys. Rev. Lett.* **1996**, *77*, 3865−3868.

(27) Polfus, J. M.; Pishahang, M.; Bredesen, R. Influence of Ce^{3+} Polarons on Grain Boundary Space-Charge in Proton Conducting Y-Doped $BaCeO_3$. *Phys. Chem. Chem. Phys.* **2018**, *20*, 16209−16215.

(28) Blochl, P. E. Projector Augmented-Wave Method. *Phys. Rev. B* **1994**, *50*, 17953−17979.

(29) (a) Henkelman, G.; Jónsson, H. A Dimer Method for Finding Saddle Points on High Dimensional Potential Surfaces Using Only First Derivatives. *J. Chem. Phys.* **1999**, *111*, 7010−7022. (b) Henkelman, G.; Uberuaga, B. P.; Jonsson, H. A Climbing Image Nudged Elastic Band Method for Finding Saddle Points and Minimum Energy Paths. *J. Chem. Phys.* **2000**, *113*, 9901−9904.

(30) (a) Henkelman, G.; Arnaldsson, A.; Jonsson, H. A Fast and Robust Algorithm for Bader Decomposition of Charge Density. *Comput. Mater. Sci.* **2006**, *36*, 354−360. (b) Tang, W.; Sanville, E.; Henkelman, G. A Grid-Based Bader Analysis Algorithm without Lattice Bias. *J. Phys.: Condens. Matter* **2009**, *21*, No. 084204.

(31) (a) Kresse, G.; Furthmuller, J. Efficient Iterative Schemes for Ab Initio Total-Energy Calculations Using a Plane-Wave Basis Set. *Phys. Rev. B* **1996**, *54*, 11169−11186. (b) Kresse, G.; Joubert, D. From Ultrasoft Pseudopotentials to the Projector Augmented-Wave Method. *Phys. Rev. B* **1999**, *59*, 1758−1775.

https://doi.org/10.1021/acsomega.2c01222
ACS Omega 2022, 7, 26107−26115

(32) Shishkin, M.; Ziegler, T. Structural, Electronic, Stability and Reduction Properties of Perovskite Surfaces: The Case of Rhombohedral $BaCeO_3$. *Surf. Sci.* **2012**, *606*, 1078−1087.
(33) Johnston, K.; Castell, M. R.; Paxton, A. T.; Finnis, M. W. $SrTiO_3$(001)(2x1) Reconstructions: First-Principles Calculations of Surface Energy and Atomic Structure Compared with Scanning Tunneling Microscopy Images. *Phys. Rev. B* **2004**, *70*, No. 085415.
(34) Richter, N. A.; Sicolo, S.; Levchenko, S. V.; Sauer, J.; Scheffler, M. Concentration of Vacancies at Metal-Oxide Surfaces: Case Study of MgO(100). *Phys. Rev. Lett.* **2013**, *111*, No. 045502.
(35) Hoffman, B. M.; Lukoyanov, D.; Yang, Z.-Y.; Dean, D. R.; Seefeldt, L. C. Mechanism of Nitrogen Fixation by Nitrogenase: The Next Stage. *Chem. Rev.* **2014**, *114*, 4041−4062.

https://doi.org/10.1021/acsomega.2c01222
ACS Omega 2022, 7, 26107−26115